JOURNAL OF GEOPHYSICAL RESEARCH, VOL. 101, NO. C6, PAGES 14,269–14,282, JUNE 15, 1996

Doppler radar measurements of wave groups and breaking waves

M. J. Smith, E. M. Poulter, and J. A. McGregor

National Institute of Water and Atmospheric Research Ltd., Wellington, New Zealand

Abstract. A 3-GHz Doppler radar has been used to study wave dynamics and backscatter from the sea surface at low grazing angles. Vertical polarization results are dominated by Bragg scatter even at low (~8°) grazing angles. Horizontal polarization results, however, show a strong upwind-downwind asymmetry with additional, high-velocity intermittent scatter in the upwind direction associated with steep or breaking waves. These characteristics have been exploited to distinguish spilling breaking events from the background Bragg scatter. While these "spikes" at a single range may appear random in time, the combined range and time information reveals a well-determined propagation pattern. It is shown that for a developing sea in deep water, group behavior modulates the occurrence of wave breaking. The frequency-wavenumber spectrum shows a clear separation between the linear dispersion curve and nonlinear effects related to breaking. The most important nonlinear feature is a line near the dominant wave group velocity which is identified with the spectrum of breaking intermittency. The slope of this line suggests that the wave components which are most likely to break lie at frequencies significantly above the dominant wave frequency.

1. Introduction

Breaking waves are believed to play an important role in air-sea exchange. This may involve the transfer of gases [*Thorpe*, 1982; *Farmer et al.*, 1993] or momentum flux [*Mitsuyasu*, 1985; *Melville and Rapp*, 1985]. Efforts to quantify the wave dissipation and mixing have been made in wave tanks using acoustic and radar techniques [*Melville et al.*, 1988], and these offer promise for field measurements. For many years an association has been made between wave breaking and sharp increases in backscattered microwave power, particularly using horizontal polarization at low grazing angles, and the events have been termed "sea spikes" [*Long*, 1974; *Lewis and Olin*, 1980; *Pigeon*, 1968]. *Phillips* [1988] attempted to quantify the association by predicting a cubic dependence on friction velocity of both the backscatter cross section and the frequency of occurrence of "spikes." *Jessup et al.* [1990, 1991] provided experimental support for this relationship from field measurements at Ku band at 45° incidence angles. Many sea spikes were not immediately associated with visible breaking [*Jessup et al.*, 1990] but were associated with specular echoes where the ratio of vertical polarization backscatter (VV) to horizontal polarization (HH), the polarization ratio, is unity. *Trizna et al.* [1991] have pointed out that the more common usage of sea spike applies to low grazing angles (< 10°) where wave tilting is unlikely to produce specular echoes and where a characteristic of the sea spikes is that HH exceeds VV.

At moderate grazing angles, resonant Bragg scatter from gravity-capillary waves is thought to be the dominant backscatter mechanism at microwave frequencies [*Wright*, 1968; *Plant and Keller*, 1990; *Poulter et al.*, 1994]. At low grazing angles, Bragg scatter from horizontal polarization for a slightly roughened sea is predicted to be ~ 30 dB below that of vertical polarization. Additional mechanisms at these angles such as wedge diffraction [*Lyzenga et al.*, 1983] and backscatter from breaking plumes [*Wetzel*, 1990] have been invoked to explain the strong observed scatter. Despite data dating back more than 20 years a satisfactory theoretical explanation of backscatter at low grazing angles remains elusive.

In this paper we investigate the properties of sea backscatter at low grazing angles (~8°) using an S band radar. At these angles, Bragg backscatter using horizontal polarization will theoretically be small. In section 3, properties of the backscatter mechanisms are sought in terms of the polarization ratio, azimuthal dependence, velocity of scatter, and temporal behavior. A key feature of the radar is the simultaneous acquisition of full Doppler spectra over a significant range extent. In section 4 the range coverage of the radar is exploited to show the propagating nature of the upwind HH backscatter. This is used to provide information on the group modulation of wave breaking of deep water waves where the breaking is predominantly spilling breaking. Finally in section 5, linear wave and group modulation information is derived from the frequency-wavenumber spectrum.

2. Experimental Description

The radar used in these studies operates at 3 GHz (λ = 10 cm) with an FMCW modulation [*Poulter et al.*, 1995a]. An adaptation using interrupted modulation (FMICW) has been developed to allow a single antenna to be switched between the transmitter and the receiver [*McGregor et al.*, 1994]. This greatly enhances the portability of the radar and facilitates

Paper number 96JC00766.
0148-0227/96/96JC-00766$09.00

Table 1. Summary of Data Sets: Wind and Wave Conditions

Data Set	Date	Figure	ψ, deg	ΔR, m	U, m s^{-1}	F, km	T_p, s	H_s, cm
SVY	May 19, 1993	2, 4	7	10	5.8	10	2.1*	21
GRC	Sept. 26, 1993	3	4	2.5	12.7	10		
SVW	June 2, 1993	4, 5	4	10	4	10	1.6*	10
PA	May 2, 1991	6, 7	4-10	2.5	5.5	7		
IB	Nov. 28, 1992	8-12	3-7	2.5	5		3.2†	

Here ψ is the grazing angle, ΔR is the range resolution, U is the wind speed adjusted to the 10-m level, F is the fetch, T_p is the period at the peak of the wave height spectrum, and H_s is the significant wave height.

* From wave gauge spectrum.

† From radar-derived spectrum.

the pointing and alignment of transmit and receive beams. For our predominantly harbor experiments, only short maximum ranges of 160-320 m were required; range resolution was varied between 2.5 and 10 m. The transverse size of a range cell on the water surface is of the order of 10 m. An absolute calibration of backscattered power has not been carried out, but relative power levels between VV and HH are consistent. The coherent radar processing scheme [*Barrick*, 1973; *Poulter et al.*, 1995a] provides full Doppler spectra for contiguous range cells with typical maximum unambiguous radial velocities of ± 2.5 m s^{-1} and a maximum Doppler velocity resolution of 0.039 m s^{-1}. For this maximum velocity resolution a sampling time of 1.28 s is required to obtain the Doppler spectra. The total backscattered power and mean Doppler velocity for each range cell are subsequently calculated from the zeroth and first moments of the Doppler spectra. The availability of Doppler spectra over many ranges is exploited to provide information on the evolution of waves.

The wind and sea conditions during the various experiments are summarized in Table 1. Most of the data to be discussed were obtained under conditions at the threshold of whitecapping, with wind speeds typically in the range of 3-8 m s^{-1} and fetches of 7-10 km. Anemometer wind speeds have been adjusted to the 10-m reference level using the correction detailed by *Smith* [1988]. All data sets except IB were obtained on Wellington Harbour at the locations shown in Figure 1a. Grazing angles were between 3° and 10° as detailed in Table 1. Since the dominant wave direction was in the direction of the wind for all data, the terms upwind and upwave are used interchangeably.

3. Doppler Velocity Results

3.1. Temporal Behavior

The usual signature of sea spikes is in the temporal behavior of backscattered power in the upwind direction [*Long*, 1974; *Lewis and Olin*, 1980]. Figure 2 shows a time series of the total backscattered power and mean Doppler velocity with a sampling interval of 1.5 s, at a single range cell for HH and VV polarizations (data set SVY). The two polarizations were recorded 8 min apart in winds of 5 m s^{-1} with the antenna pointed directly into the wind and waves. In these conditions with the 10-m range resolution, the dominant 2.1-s period waves were not resolved. The backscattered power for HH exhibits the classic signature of sea spikes [*Long*, 1974] with strong intermittent peaks, in contrast to the more moderate variations on VV. Although the mean level of the VV return exceeds that of HH by a factor of 7, the peak values of HH greatly exceed those of VV. This is in contrast to the specular-type echoes frequently seen at moderate grazing angles (~45°) where HH seldom exceeds VV [*Jessup et al.*, 1990]. Whereas the VV return typically varies by a factor of less than 2, the HH returns exhibit extreme fluctuations as large as 10-100 times the mean power. The ratio of the standard deviation to the mean of backscattered power also reflects this spread: for VV it is typically 0.3,

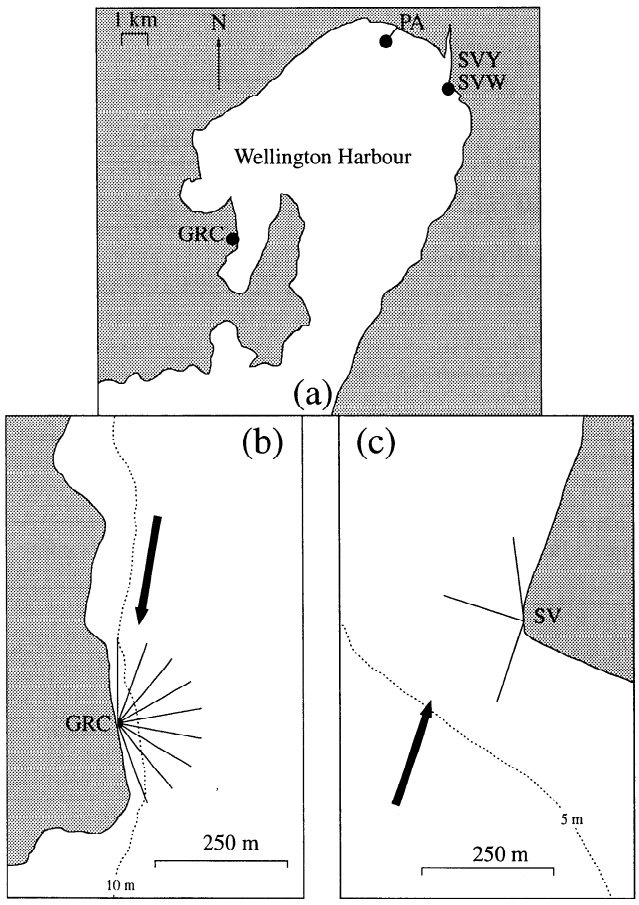

Figure 1. (a) Locations of the radar sites within Wellington Harbour. (b) Detail of GRC site. The thin lines show the antenna pointing directions during the scan. (c) Detail of the SVY and SVW site. The thin lines show the upwind, downwind (SVY), and cross-wind (SVW) antenna pointing directions. The thick arrows show the wind direction. Depth contours are shown by the dotted lines.

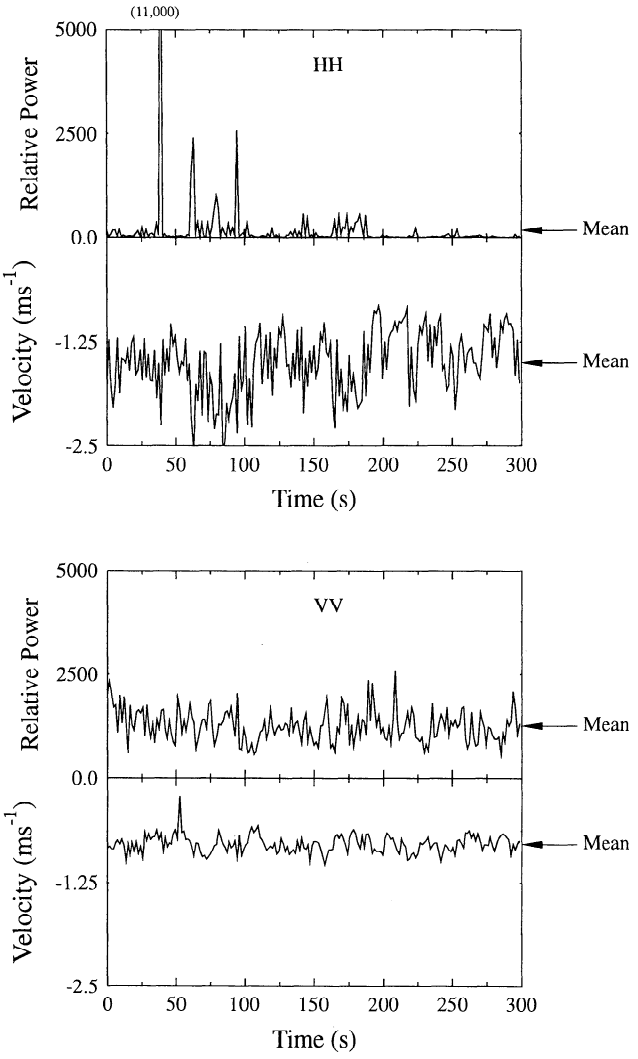

Figure 2. Temporal variation of backscattered power and velocity for (top) horizontal (HH) and (bottom) vertical (VV) polarization with the antenna directed upwind. Markers indicate mean power and velocity levels. Wind speed was 5.8 m s^{-1}.

while for HH it is 4. In the following sections we will show that the VV return is largely consistent with Bragg scatter. The backscattered power will be the sum of the separate contributions from Bragg scatter and sea spikes [*Phillips*, 1988]. Although simultaneous VV and HH data are not available here, we can infer that the HH spikes greatly exceed similar events on VV (either in strength and/or duration), because the VV return is not enhanced above the background (Bragg) contribution by an equal amount. Figure 2 also emphasizes the strong polarization difference in the time series of velocity. HH velocities are much larger in magnitude and also have a larger variance than VV. The spikes (e.g., at times of 39 s and 63 s) also often coincide with the largest negative Doppler velocities, which in the present radar configuration correspond to velocities from the region near wave crests.

3.2. Azimuthal Scan

The azimuthal dependence of the velocity difference between the polarizations is now examined. For the GRC data set the direction of the antenna was scanned from upwind to downwind in 20° increments, as indicated in Figure 1b, with 1 min at each azimuth. The measured velocities are shown in Figure 3, where the horizontal axis denotes both time and azimuth in 20° steps, with zero degrees corresponding to the antenna directed upwind. The grazing angle for these measurements was 4.4°. Since the measurements were taken from a land-based site, some sheltering may affect the velocities at the extreme ends of the azimuthal scan. Mean velocities were obtained from the first moment of the raw Doppler spectra, and in Figure 3, 20 velocity data points have been averaged to reduce the scatter. The average wind speed at this time was 12.7 m s^{-1} over a fetch of 10 km, with gusts to 19 m s^{-1}.

The largest radial velocities in Figure 3 occur in the upwind direction. In this direction, horizontal polarization velocities exceed those of vertical polarization by a significant amount, 1.1 m s^{-1} (a factor of 2). This differential velocity decreases as the azimuth increases, until downwind the difference is within the range of data scatter. The HH scan was measured 18 min after the VV scan, during which time the mean wind speed had decreased by 0.7 m s^{-1}. Thus the higher sea surface velocity using HH polarization cannot be attributed to increased wind stress.

A significant feature of Figure 3 is that the VV return has a cosinusoidal variation with azimuth symmetrical about zero velocity. This would occur for a simple model of radar backscatter dominated by Bragg scatter plus advection by a background current in the wind direction. In this situation, and assuming waves with angular distribution $\cos^4(\theta/2)$, the mean velocity variation with azimuth will be cosinusoidal with an amplitude of $V_b + V_c$ and a zero offset [e.g., *Poulter et al.*, 1995b]. Here V_b and V_c are the intrinsic Bragg phase velocity of the scatterers (0.29 m s^{-1}) and the surface background current, respectively. A cosine variation plus an offset has been fitted to the VV velocities in Figure 3, as shown by the dotted curve. The cosine has an amplitude of 1.08 m s^{-1} (standard deviation 0.04 m s^{-1}), an offset of -0.12 m s^{-1} (stan-

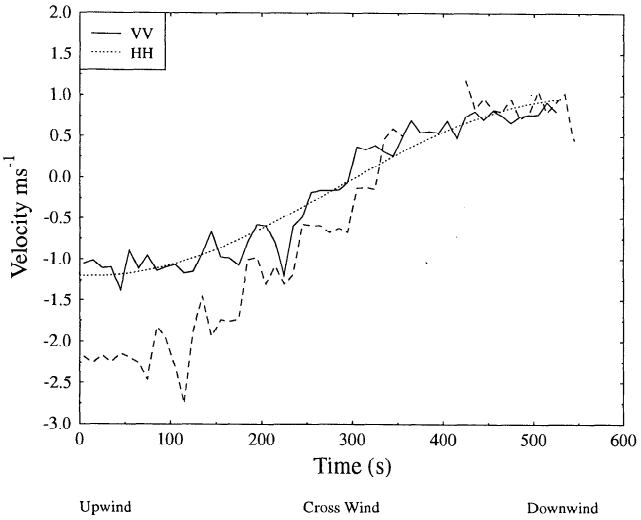

Figure 3. Mean velocity versus time as antenna azimuth relative to wind is stepped from the upwind direction to downwind for vertical polarization (solid curve) and horizontal polarization (dashed curve). Dotted curve is the least squares fit of a cosinusoidal variation to the vertical polarization velocity.

dard deviation 0.06 m s^{-1}), and a phase within 7° of the measured wind direction. After subtracting the Bragg velocity, the implied surface current is 0.79 m s^{-1}. These measurements were taken in an enclosed arm of the harbor where bulk and tidal currents are small. Hence the surface currents will be dominated by wind drift. *Wu* [1975] predicts a surface drift of 3.5 % of wind speed, or 0.44 m s^{-1} for the 12.7 m s^{-1} wind speed, while *Lange and Hühnerfuss* [1978] give a broader range of 2.6 to 5.5 %, based on field measurements, i.e., 0.33 m s^{-1} to 0.70 m s^{-1}. Our deduced velocity (0.79 m s^{-1}) lies just beyond the upper end of this range. Some bias of the measured value can be explained by wave shadowing. For the waves generated in the 13 m s^{-1} wind speeds, and for the grazing angles used in Figure 3, shadowing may bias Doppler spectra toward crest velocities of the larger scale waves within the range cell. We have modeled this effect using the wave spectral form of *Donelan et al.* [1985], with the appropriate wind speed and fetch. The geometrical shadowing is predicted to result in a current bias of 0.25 m s^{-1}, which brings the current into the middle of the range of the *Lange and Hühnerfuss* [1978] results. The cosine fit to the data also has an offset of -0.12 m s^{-1}. This suggests a small azimuthally asymmetric contribution to the VV scatter, such as a much weaker contribution from the mechanism which clearly occurs with upwind HH polarization and which is possibly associated with wave breaking. Accordingly, for data at lower wind speeds where effects such as breaking are less frequent (e.g., 5 m s^{-1}), the VV dc offset is found to be correspondingly less (0.06 m s^{-1}). Additional influences such as shadowing or sheltering from the wind at the end of the scan may also have had some effect.

We conclude that when shadowing is taken into account, the azimuthal variation of VV velocities is consistent with a model of Bragg backscatter plus a wind drift current. In contrast, the HH variation in the upwind direction has a strong additional velocity component which cannot be explained by the Bragg model, while in the downwind direction it is similar to Bragg scatter.

3.3. Doppler Spectra

Having established that a clear difference in velocity exists between VV and HH, at least in the upwind direction, we now look at the Doppler spectra, which provide a greater level of detail than the mean velocities. The Doppler spectra from data sets SVW and SVY (Figure 4) are incoherent averages of 200 individual spectra spaced at 1.5 s, with a velocity resolution of 0.039 m s^{-1}. To maintain radar frequency independence, Doppler information is presented in terms of Doppler velocity. A range resolution of 10 m allowed the radar to achieve optimal velocity resolution, but as in section 3.2, it does not allow individual crests to be resolved. The VV and HH spectra were obtained sequentially within 15 min of each other. For the HH measurements, the radar sensitivity was increased by 10 to 15 dB. This has been corrected for in the figures, but it does contribute to a difference in noise floors between VV and HH spectra. The azimuthal dependence of scattering gives rise to the three distinct situations that are illustrated in Figure 4: with the antenna directed cross wind, downwind, and upwind.

In Figure 3 we showed that the VV velocities were largely consistent with Bragg scatter plus a wind drift current. The ideal situation to unambiguously identify Bragg scatter is in

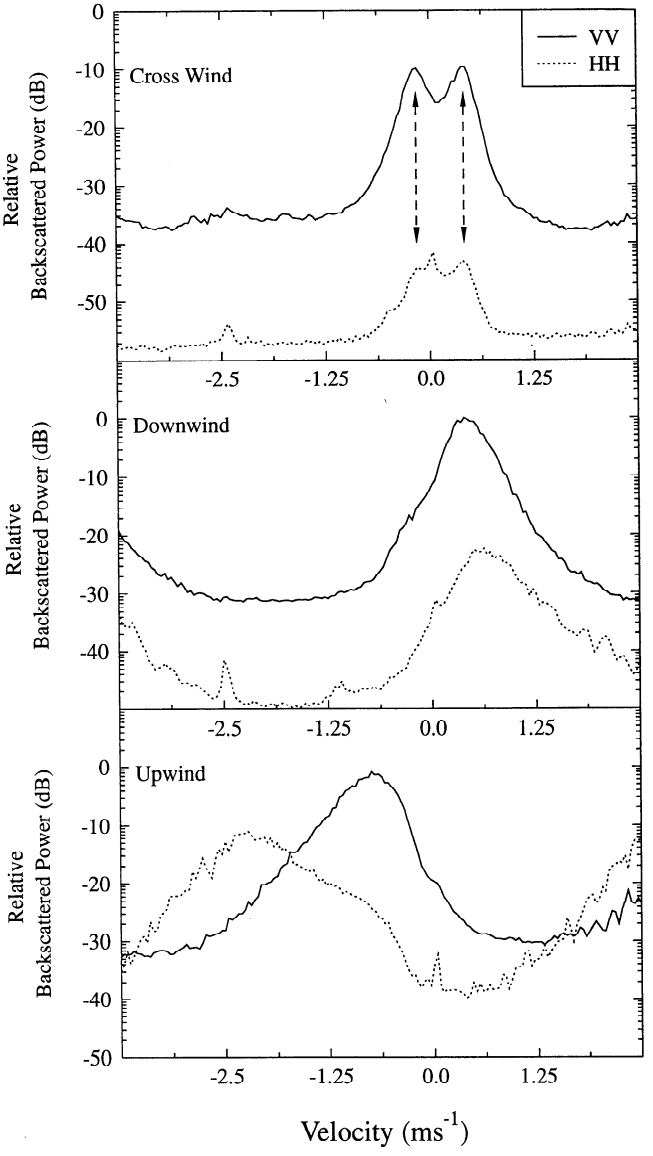

Figure 4. Average of 200 Doppler spectra in a single range cell for vertical polarization (solid curve) and horizontal polarization (dotted curve), with the radar directed (top) cross wind, (middle) downwind, and (bottom) upwind. The dashed lines in the top panel indicate the position of the Bragg peaks. The increasing power toward the sides of the panel is discussed in the text. Negative velocities are toward the radar.

the cross-wind direction where the advancing and receding Bragg waves ideally give rise to a Doppler spectrum with two equal peaks separated by twice the Bragg wave phase velocity. A second advantage of the cross-wind situation is that other scattering contributors, such as wedge and breaking effects, will be at a minimum due to geometrical considerations. The mean wind speed for this SVW data set was 3.5 m s^{-1} (with standard deviation 0.8 m s^{-1}), and the mean value of friction velocity was 0.09 m s^{-1}, as measured by a sonic anemometer mounted within 150 m of the radar footprint. A wire wave gauge was used to monitor wave conditions, and the resulting wave height spectrum showed wind waves with a peak period of 1.6 s.

The cross-wind spectra for VV (top panel of Figure 4) provide convincing evidence of Bragg scatter, with two peaks

separated by 0.57 m s^{-1}, which is close to the theoretical value of 0.59 m s^{-1}. The peaks are broadened due to the orbital velocities of longer-scale unresolved sea waves [*Plant and Keller*, 1990]. We have measured similar cross-wind dual peaked spectra with a spacing of $2V_b$, in conditions with similar fetch in wind speeds up to 6 m s^{-1}.

The HH cross-wind spectrum also has dual peaks but at ~33 dB lower level. The positions of the two HH peaks are indicated by the vertical dashed arrows to distinguish them from the clutter at zero velocity. Although clutter from nearby stationary objects has been suppressed, a remnant is still visible in all three panels. Before attributing the dual HH peaks to horizontally polarized Bragg scatter, it must be recognized that at such low levels, imperfections in the alignment of the antenna feed (in this case a slotted dipole) can result in transmission and reception of a small component of the orthogonal polarization. The uncertainty in the physical alignment of the antenna polarization angle in this data set is estimated to be between 1° and 2°. For polarization independent scatter, the error would be small, varying as $\tan^4 \varepsilon$, where ε is the angular error in alignment. However, the strong anisotropy of Bragg scatter between HH and VV [*Wright*, 1968] makes reception of horizontal polarization very sensitive to tilting out of the plane of incidence, whether it occurs at the antenna, or on the sea surface due to wave slope, particularly at these low grazing angles. The estimated "crosstalk" resulting from the small component of VV transmitted due to antenna alignment error is ~ -30 dB. Thus physical limitations of the antenna establish a lower limit to the significance of the HH return. In this case, what can be said is that in this low sea situation the HH Bragg returns are at least 30 dB down on the VV returns. From composite surface theory, this then implies a very low value of wave slope variance in the cross-wind direction. All other HH data in this paper were obtained under larger wave slope conditions, resulting in higher horizontal polarization scattering levels. For the strong wind data in Figure 3, for example, the HH backscattered power level was at most 15 dB below that of VV.

The data with the radar directed in the downwind and upwind directions (Figure 1c) were obtained under slightly stronger wind conditions of ~5.8 m s^{-1} with the same fetch (data set SVY in Table 1). The peak period from the wave gauge was 2.1 s with a significant wave height of 0.21 m. The downwind VV spectrum (middle panel of Figure 4) is dominated by a single peak offset from the origin, consistent with Bragg scatter from 5 cm waves receding from the radar. The velocity offset of the peak (0.41 m s^{-1}) will be a combination of the Bragg scatterer phase velocity (0.29 m s^{-1}), advection due to surface currents, which will include wind drift and flow from a nearby river, and any bias due to shadowing removing the contribution of trough orbital velocities. The wind drift term, after correcting for the angle between the antenna and the exact downwind direction, is expected to be 0.2 m s^{-1} using 3.5% of wind speed. So the combined contribution of Bragg phase velocity and wind drift (0.49 m s^{-1}) accounts for the bulk of the measured value. The spectral width is measurably wider than the cross-wind spectrum in the earlier lighter wind conditions, reflecting the larger wave orbital velocities.

The HH Doppler spectrum peak is again at a much lower power level (by 22 dB). From the composite surface model [*Wright*, 1968], a slope variance of 0.01 would be needed to give this polarization ratio. The downwind HH spectrum shows two less obvious differences to the VV spectrum. First, the HH peak velocity is displaced a further 0.17 m s^{-1} from the VV. Although a change in background currents or wind drift in the time between recordings (7 min) cannot be completely discounted in this particular data set, additional data sets also show such an offset, indicating the influence of a more fundamental difference in scattering mechanism. Initial investigation of this differential velocity shows that it increases with wind speed but is also dependent on fetch. If it is assumed that Bragg scatter is the dominant backscatter mechanism for both HH and VV downwind, the result implies that a greater proportion of the scatter occurs closer to the underlying long wave crests (where the orbital velocity is largest in the line of sight) for HH than VV; that is, the phase of the modulation transfer function is closer to 0° for HH than VV at wave frequencies ~ 0.5 Hz. The HH spectrum is also markedly more asymmetric, with proportionally more scatter at the higher velocities.

The upwind spectra (bottom panel of Figure 4), which were taken under similar wind conditions, show the largest contrast in shape between VV and HH. The VV spectrum shows the dominant features of Bragg scatter (with scatterers moving toward the radar), but with a larger peak velocity offset (-0.69 m s^{-1}) than downwind and an increase in occurrence of scatter at high velocities (-2.5 to -1.25 m s^{-1}) as evidenced by the asymmetric spectrum. A possible reason for the larger offset is that enhanced roughness on the forward face of long waves results in enhanced scatter there, as described by the modulation transfer function [*Plant et al.*, 1983]. This may bias the upwind results to the higher line of sight orbital velocities near the crest, while in the downwind direction this enhanced scatter region is shadowed. Although there is only a modest change in the upwind VV spectrum compared to downwind, the change in HH is very marked, with the power 13 dB higher than HH in the downwind case, strongly skewed, and with the dominant power at a much greater velocity (-2.2 m s^{-1}). Velocities are well above the values expected from the orbital velocities of the underlying dominant waves (< 0.9 m s^{-1}) but instead approach the phase velocity of the dominant waves (-3.3 m s^{-1}), as also observed by *Keller et al.* [1986]. The averaged HH Doppler spectra also clearly have a wider bandwidth than in the downwind situation. One consequence of the FMCW processing scheme is that for each range cell, velocities greater than the radar maximum velocity parameter spill into the Doppler spectrum of the adjacent range cell. Thus the rising HH power level to the right of the bottom panel is simply due to the velocity magnitude of the next range cell exceeding 2.5 m s^{-1}, the maximum unambiguous velocity, and can be ignored here.

The characteristics of high velocity and intermittency could be produced by scatter from the breaking crest or from scatterers trapped ahead of a steep breaking wave front. The fact that only a small effect is seen in the downwind direction implies a strong geometrical dependence, such as reflection provided by the toe of a breaker observed from the upwind position [*Wetzel*, 1990]. The horizontally polarized returns therefore provide a sensitive indicator of wave breaking, particularly at these grazing angles.

3.4. Residual HH Doppler Spectra

Although the HH upwind spectrum is dominated by a peak at higher velocities than VV, there is evidence of a change

in the slope of the average HH spectrum near -0.7 m s^{-1} where a Bragg peak would be expected. This suggests that there may be residual underlying Bragg scatter. In order to examine this in more detail, individual HH spectra have been selected and averaged only when the HH spikes were absent based on a combined amplitude and velocity threshold. The criterion used to identify a spike event was if the total power within a range cell exceeds the data set average by 3 dB or the velocity exceeds 1.5 times the data set average velocity. (The velocity condition was introduced to account for spectral leakage from exceptionally large spikes at other ranges.) Unlike the spike data, this residual did not show large variations in time. The selection process was facilitated by using data at low wind speeds where the spike occurrence frequency is less [*Phillips*, 1988]. An average of 34 such spectra is shown by the solid line in Figure 5, while the mean of all HH spectra is shown by the dashed line. The VV/HH ratio is now 25 dB, which is comparable to the downwind ratio under similar wind conditions. It is clear that the breaking events are a disjoint distribution at high velocities. In anticipation that the HH residual may be of Bragg origin, the (Bragg dominated) VV return is also shown on a larger scale (dotted line). However, we find that the nonspike HH upwind return has contributions at distinctly higher velocities than the VV return but below the typical spike velocities. Possible reasons for this are either a significant polarization dependence of the modulation transfer function or a different mechanism which is neither Bragg nor breaking waves.

3.5. Discussion

The experimental results in this section can be summarized as follows:

1. The presence of VV dual peaks separated by twice the Bragg velocity in cross-wind conditions is a strong indicator of Bragg scatter.

2. The VV downwind and upwind data are also consistent with Bragg scatter plus advection by currents largely of wind drift origin.

3. In the cross-wind direction the HH spectrum has not been adequately resolved due to antenna alignment uncertainties, but in the downwind direction it is similar to VV although at a much lower power level; that is, it is consistent with Bragg scatter both in terms of Doppler shift and polarization ratio. However, small but consistent differences in spectral shape also exist.

4. The greatest difference is in the upwind direction where additional strong but intermittent scatter at high velocity skews the mean spectrum strongly. Although the mean level is lower than VV, during spike events, HH backscatter exceeds that with VV polarization. This feature distinguishes the scatter at these lower grazing angles from that at more moderate angles where wave tilting can result in specular reflection with equal VV and HH return [*Jessup et al.*, 1990].

A wedge scattering model was formulated by *Lyzenga et al.* [1983] which augmented the HH scatter at low grazing angles. Wedge-like wave crests certainly occur, but since the theoretical polarization ratio is again below unity at low grazing angles (< 10°), this theory cannot explain our strong HH contributions. Scatter from symmetrical wedges would also not explain the large upwind/downwind difference observed.

Parasitic capillary waves have been shown to be strongly generated on the forward face of steep gravity waves [*Longuet-Higgins*, 1963; *Duncan et al.*, 1974] which would give enhanced Bragg scatter there. Their scale is generally < 1 cm, whereas the wavelength required for Bragg scattering in the present experiments is ~ 5 cm. Alternatively, *Banner and Fooks* [1985] suggested that the breaking zone was a source of Bragg waves. But again Bragg scatter would be expected to be greater for VV than HH and therefore cannot account for the strong HH backscatter of the breaking wave spikes. The lifetime of Bragg scatterers would also be longer than the intermittent features observed.

A related possibility is microscale breaking where very short gravity waves break but because of their small scale, surface tension prevents air entrainment [*Banner and Peregrine*, 1993]. Although frequently observed, their relative contribution to radar backscatter is largely unknown. If microscale breaking is important here, the high Doppler velocity of the observed dominant scatter would require such breaking waves to be bound to the larger-scale waves whose phase velocity would be appreciable. There remains the problem of obtaining the strong backscatter with HH polarization.

A recent theoretical development by *Wetzel* [1993] suggests that large curvature features of the sea surface are sufficient to give strong backscatter, without the need for Bragg resonance at all. Such features will travel with the wave and will not have the additional Bragg wave phase velocity. The harbor VV results, however, continue to support Bragg scatter in general, but this high curvature mechanism may well be relevant to the upwind HH spikes. Experimental support for an association of the spike backscatter with large curvature has been given by *Trizna et al.* [1993] in wave tanks. The inclusion of polarization effects and the estimation of actual scattering cross sections in Wetzel's model are required to test its applicability.

The breaking plume model of *Wetzel* [1990] comes closest to representing many of the features of the sea spikes. For small plumes (i.e., with radii ~ λ) such as were present in the light wind conditions here, the plume model can produce polarization ratios of -10 dB close to the wave crest for low grazing angles. Further, the HH return is predicted to be of a more "spiky" nature than VV. Shadowing effects which

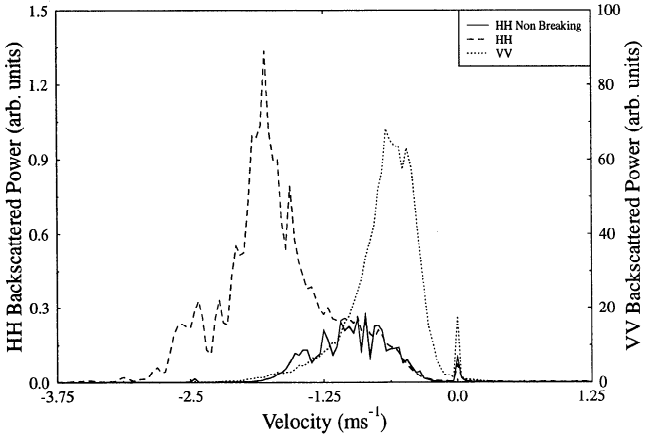

Figure 5. Averaged HH Doppler spectrum using all data (dashed line) and data selected to be free of spikes (solid line). For reference the VV Bragg return is shown on a larger scale (dotted line).

make the wave troughs less visible than the crests will also emphasize the strong HH return. Since the toe of the plume will only be observed looking upwind, the lack of response looking downwind is also consistent. The speed of the plume however, might be expected to be at least as great as the underlying wave phase velocity as the plume accelerates down the front face, but the observed velocities are less than the dominant wave phase velocity. One explanation for this is if the most prominent breaking waves in a wind-wave spectrum are at frequencies higher than the spectral peak [*Donelan et al.*, 1985], since these waves would have a lower phase velocity. We show additional evidence that this is the case in section 5.

4. Group Modulation of Wave Breaking

The largest HH backscatter has long been associated with whitecapping at low grazing angles [*Lewis and Olin*, 1980]. For the following data set we have also visually related the strong HH spikes with breaking waves. Although the time series of HH backscatter at a single range cell (e.g., Figure 2) has a somewhat random appearance, if the association of spikes with breaking (or near breaking) waves is valid, the sea spike features may exhibit a propagating characteristic. In this section we exploit the range coverage of the FMCW radar to examine these propagation effects.

Individual Doppler spectra are shown for nine contiguous range cells of data set PA in Figure 6. The data sampling interval was 0.4 s with a range resolution of 2.5 m and a velocity resolution of 0.16 m s^{-1}, along a single narrow azimuth looking into the direction of wave propagation. Useful data were obtained at this site from ranges of 50 to 150 m. The data were recorded under steady wind conditions of 5.5 m s^{-1} over a fetch of 7 km. The resulting short wavelength waves, O(5 m), can be treated as deep water waves for the 5-m water depth. In these conditions, individual wave profiles cannot be resolved in the mean velocities, but intermittent propagating features are still apparent. The breaking events for the 45° polarized returns in the upper panel are largely obscured by the dominant Bragg backscatter (45° polarization is used as representative of vertical polarization, which could not be recorded in this experiment.) There is only moderate variation in backscattered power with time, and the mean velocity is small. (The decrease in power at the lower ranges results from the projection of the antenna pattern on the water surface.) In contrast, breaking waves dominate the spectra for HH polarization in the lower panel. The breaking is characterized by higher velocities (~2 m s^{-1}) than Bragg scattering velocities, as in Figure 2, and there is a clear propagation toward the radar (decreasing range with increasing time). Close examination reveals that as the breaking region propagates, it is intermittent, with strong returns lasting for two to three time intervals (0.8-1.2 s) spaced 3.2 s apart.

The overall propagating nature can be seen more clearly in Figure 7 where a 1.5-min segment of the range and time distribution of backscattered power for HH is shown. Since the power for HH is predominantly associated with breaking waves, it is indicative of the distribution of whitecapping. Spectral windowing applied to the raw data has spread the returns in range by a factor of 1.5. A clear feature of the breaking events is the regular pattern of breaking, with clustering into "groups" which propagate toward the radar. Some of these groups are quite coherent; the longest lived was tracked for 80 m (i.e., of the order of 20 wavelengths). The speed of propagation of each group is fairly consistent (1.1-1.4 m s^{-1}), but the separation between individual groups is seemingly irregular. Another feature evident in Figure 7 is the periodic nature of the breaking within each group, also seen in Figure 6. For the marked example in Figure 7 (solid lines, lower left), the breaking of a crest recurs at a time interval of 3.2 s, at a spatial position 3.7 m downstream.

An explanation for these characteristics can be found in the group nature of narrow band wave propagation [*Donelan et al.*, 1972]. The wave packet formed in this situation propagates at the group velocity which for deep water waves is half the phase velocity of the central frequency wave. Wave breaking will tend to occur when each individual wave crest moves through the wave packet and nears the center of the envelope where the wave height and slope, and hence instability, are greatest. Breaking will cease when the wave amplitude reduces below the breaking threshold (see Figure 1 of *Donelan et al.* [1972]). The breaking will repeat when the next wave crest in the group approaches the center of the envelope. Since the velocity of the crests relative to the envelope is half the phase velocity, patterns of breaking would be expected to repeat at time intervals of twice the wave period and be spaced downstream by one wavelength. This phenomenon has been observed visually from the air [*Donelan et al.*, 1972], in wave tanks, and in underwater bubble clouds [*Thorpe and Humphries*, 1980; *Farmer and Vagle*, 1988] but to our knowledge has not been measured by radar before.

Our radar data fit this model well. For the example marked in Figure 7 with solid lines, the measured time interval of 3.2 s between the breaking of successive crests implies a breaking wave period of 1.6 s. The group velocity of such deep water waves is 1.3 m s^{-1}, in good agreement with the value of 1.2 m s^{-1} calculated from the motion of the envelope of breaking. A 1.6 s wave would also have a wavelength of 4 m in deep water, in agreement with the measured value of 3.7 m. We can give physical meaning to the duration of radar measured breaking events when, as here, the breaking wave can be tracked over many range cells. On a short timescale (~ 1 s) the duration of the spike measures the duration of breaking of a single crest, which will depend on the degree of wave instability. On a longer timescale (~tens of seconds), the duration of the sequence of breaking events measures the lifetime of the unstable wave group, provided the radar has sufficient spatial coverage.

5. Dispersion Relationship Diagrams

5.1. Range-Time Display

In the previous section the radar spatial resolution was insufficient to distinguish individual wave crests. We now consider a wave field with a dominant wavelength (~16 m) which is significantly greater than the 2.5-m range resolution. The data set IB was recorded in McMurdo Sound, Antarctica, under light wind conditions (~5 m s^{-1}) with a developing sea on water of 800-m depth. The sea was incident upon a fast ice boundary where the radar was located. In order to increase the elevation angle, the radar antenna was mounted on a 14-m-high tower and aligned into the direction of wind and wind waves. A useful range coverage of 130 m was obtained in this configuration. The time resolution was 0.3 s.

Figure 8 shows a section of the backscattered VV power as a function of range and time after a correction has been

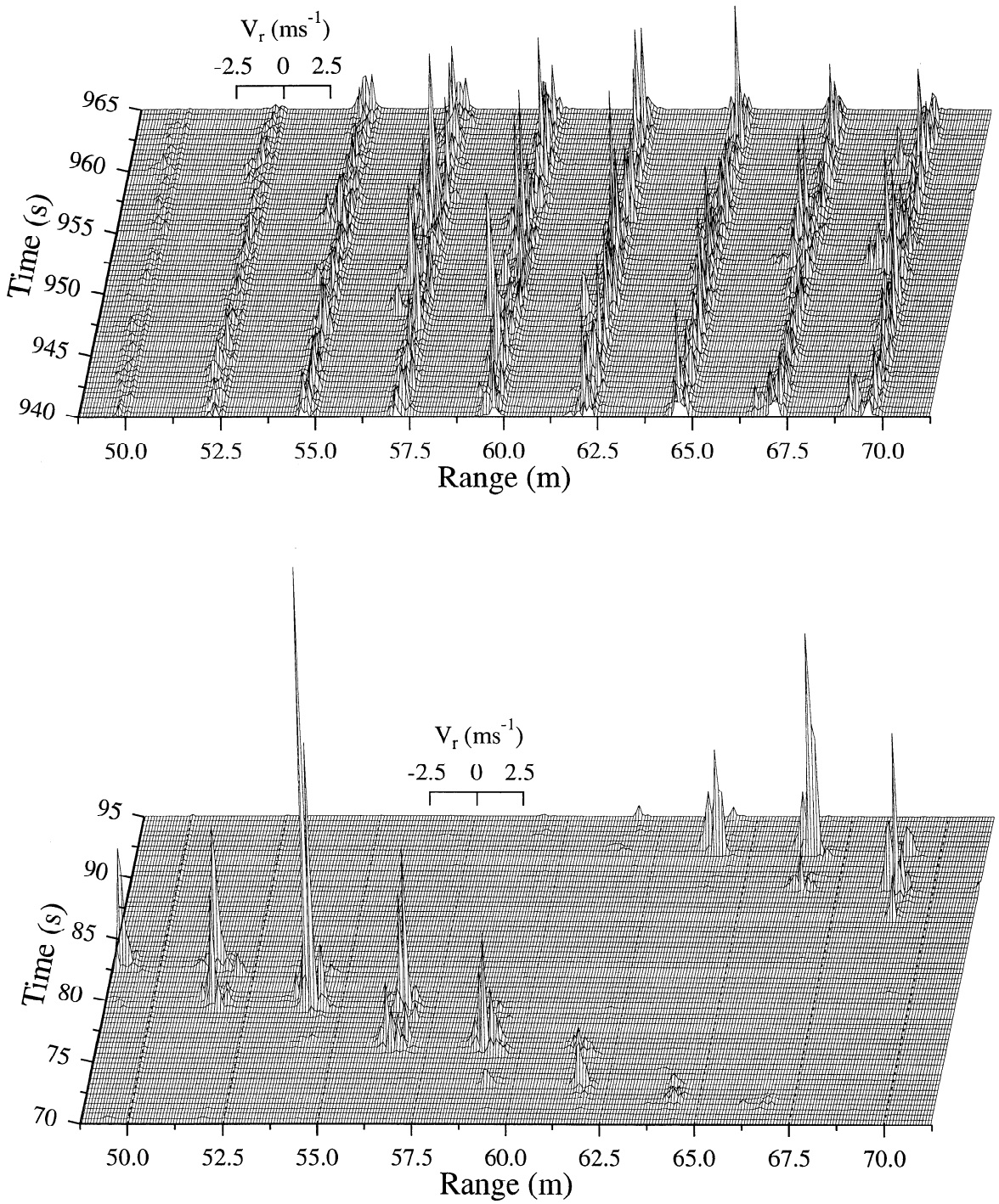

Figure 6. Doppler spectra for nine adjacent 2.5-m range cells at 0.4 s time intervals. Zero radial velocity at each range cell is shown by the dotted line at the range markers. The upper panel, obtained using 45° polarization, is also representative of vertical polarization. In the lower panel, obtained using horizontal polarization 15 min earlier, bursts of backscattered power reveal a group of spilling breaking waves propagating toward the radar. The scale of backscattered power is a factor of 5 larger for horizontal polarization.

made to compensate for the projection of the antenna pattern on the water surface. Regions of enhanced backscattered power, corresponding to wave crests, can be seen propagating toward the radar. The superimposed solid lines emphasize a set of wave crests as they approach the radar. From the diagram these waves have a period of 3.1 s and a phase velocity of 5.1 m s^{-1}. In addition, a group modulation of backscattered power can be seen propagating at a slower velocity. An example is highlighted by the single solid line. The velocity of this feature is 2.5 m s^{-1}, which corresponds closely to the theoretical group velocity for these deep water waves, further indicating the importance of group effects in wave development. This particular data set was primarily obtained as part of a campaign to study the transfer of ocean

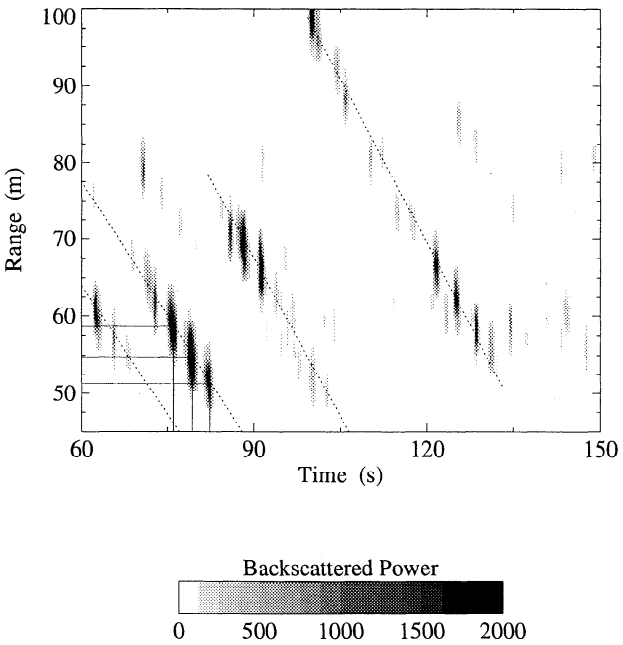

Figure 7. Range and time variation of total backscattered power within each range cell, using horizontal polarization, representing the occurrence of wave breaking. Dotted lines indicate the propagation of wave groups. Solid lines show the range and time intervals between the occurrence of breaking crests within a group. Waves are not spatially resolved.

wave energy into wave modes in the ice. These ice-coupled waves, measured by strain gauges set in the ice, also showed this strong group modulation.

5.2. Linear Dispersive Features

A two-dimensional Fourier transform of such a power or mean velocity image yields the frequency versus wavenumber dependence of the waves, i.e., the dispersion relationship. The power spectrum using velocity data is shown contoured in Figure 9. The wavenumber axis is the radial component of the wavenumber parallel to the radar pointing

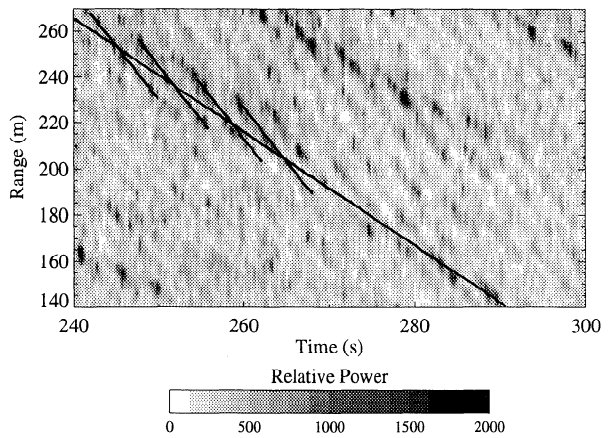

Figure 8. Image of the variation of backscattered power for resolved waves, corrected for antenna pattern effects. The set of short solid lines outlines the propagation of 3.1-s waves toward the radar. The single line shows an additional modulation propagating at the group velocity.

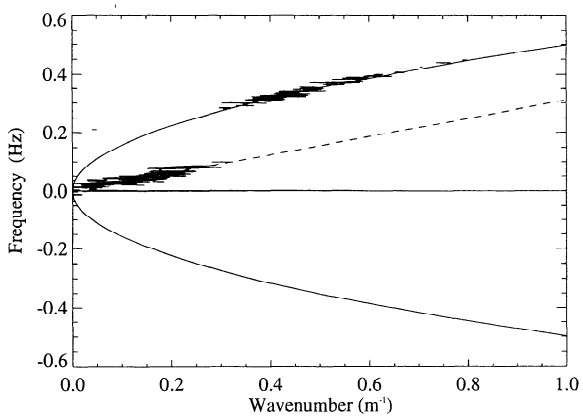

Figure 9. Contour plot of frequency-wavenumber spectrum of velocity using vertical polarization. The upper half of the diagram represents waves traveling toward the radar, and the lower half represents waves traveling away. Spectral power is concentrated along the linear dispersion relation (solid line) and also along the group line (dashed line) which represents the group velocity of waves centered at 0.4 Hz.

direction. In this diagram the contours are narrow in frequency but wide in wavenumber, reflecting the greater sampling rate and length of series in the time domain. The resolutions are 0.0016 Hz and 0.044 rad m^{-1}. An attractive property of the two-dimensional space-time transform is that advancing and receding waves fall into separate quadrants, shown as positive and negative frequencies in Figure 9. In the present geometry, the receding waves would correspond to reflections from the ice edge at the radar site. The plotted dispersion line (solid curve) is given by

$$2\pi f = \left[\frac{gk_r}{\cos\theta}\tanh\left(\frac{k_r h}{\cos\theta}\right)\right]^{\frac{1}{2}} + \frac{k_r}{\cos\theta}U_C\cos\alpha \qquad (1)$$

where f is the ocean wave frequency, k_r is the ocean wave wavenumber determined along the radar line of sight, h is the water depth (800 m), and θ is the angle between the radar pointing direction and the propagation direction of the waves. The second term accounts for advection of waves by currents of magnitude U_c and direction α with respect to the waves; U_c and α are set to zero in the figure. The lower solid curve is the dispersion curve for waves traveling away from the radar.

The spectrum is dominated by two features. First, above a wavenumber of 0.3 rad m^{-1} the contours of spectral density lie close to the theoretical linear dispersion curve. An additional feature extends from the origin following an approximately linear relationship between frequency and wavenumber. We have labeled this feature the "group line" for reasons given below.

The dispersive feature peaks at $f = 0.32$ Hz, $k_r = 0.41$ rad m^{-1}, consistent with the spot estimates from Figure 8. The waves contributing to the dispersion line have a direction predominantly along the radar line of sight, since off-axis waves are strongly discriminated against when the ocean wavelength is smaller than the width of the antenna footprint on the sea surface. In this situation, different phases of a wave cycle occur simultaneously within a given range cell and therefore cancel. The radar footprint for Figure 9 was centered at a range of 165 m, and with the 5.8° -3 dB beam

width, the horizontal size of the footprint is 17 m. Thus waves with $k > 0.37$ rad m^{-1} will be increasingly attenuated from off-axis directions.

Close examination of the high wavenumber components in Figure 9 shows a small but consistent displacement above the dispersion line with $\theta = 0$ and $U_c = 0$, implying the presence of a current. The best fit by eye of the data to the dispersion curve was obtained with a current of 0.1 m s^{-1}. Currents can arise from several sources: wind drift, Stokes drift, tidal currents, or oceanic currents. The shortest wavelengths may also be affected by the orbital velocities of long scale waves, if they are strained preferentially at long wave crests [e.g., *Irani et al.*, 1986]. In confined waters, wind drift is believed to occur in a very thin layer of the ocean surface, and although capable of Doppler shifting the short Bragg scatterers, it is unlikely to strongly influence the larger-scale ocean waves in Figure 9 which extend over greater depths. *Wu* [1983] has argued that the major contribution to the Stokes drift comes from waves near the peak of the wind-wave spectrum. The present wave spectrum peaks at $k_r \sim 0.4$ rad m^{-1}; thus the Stokes drift which has an exp(-2kz) fall off with depth below the surface (z) will extend over a depth of ~ 1 m. The expected magnitude of the Stokes drift for the estimated fetch of 35 km and wind speed of 5 m s^{-1} is 0.12 m s^{-1} [*Wu*, 1983] in good agreement with the fit to Figure 9.

5.3. Nonlinear Features

The nonlinear feature in Figure 9 has two significant characteristics: (1) the spectral density is concentrated at low frequencies and wavenumbers and (2) the spectral density is approximately linear with a slope (2.0 m s^{-1}) which is close to but smaller than the group velocity of the spectral peak (2.5 m s^{-1}). If the line is interpreted as a group velocity, it implies a central frequency of 0.4 Hz. Assuming that the feature is related to the wave spectrum, its origin requires some nonlinearity in either the hydrodynamics or scattering processes. The wave group modulation of wave height will not in itself result in power lying off the linear dispersion relation curve, since the wave group simply represents a linear superposition of component waves within a narrow band. The most visibly obvious source of nonlinearity is from breaking waves. As we have seen, the breaking results in sudden enhancements both in backscattered power and in scatterer velocities near the crests, and these enhancements are modulated by the group behavior of the dominant waves, with intermittent breaking features traveling at the group velocity. From section 4, we would also expect the enhancements to be more apparent using horizontal polarization, since HH is both more sensitive to breaking and has a lower level of Bragg scatter. This is confirmed in Figure 10, which shows the frequency-wavenumber spectrum of velocity using HH polarization. As expected, the group line dominates, with little spectral power along the dispersion curve. The additional sideband-like features will be discussed in section 5.4. As with vertical polarization, the slope of the line is the group velocity for a group of waves centered at 0.4 Hz.

A second source of nonlinearity that is relevant in these low grazing angle measurements is shadowing. The highest waves of a group will be preferentially illuminated and contribute to the backscatter. Again, these features will propagate at the group velocity [*Wetzel*, 1978]. However, we expect this effect to produce a weaker modulation of both power and velocity than produced by breaking, because while

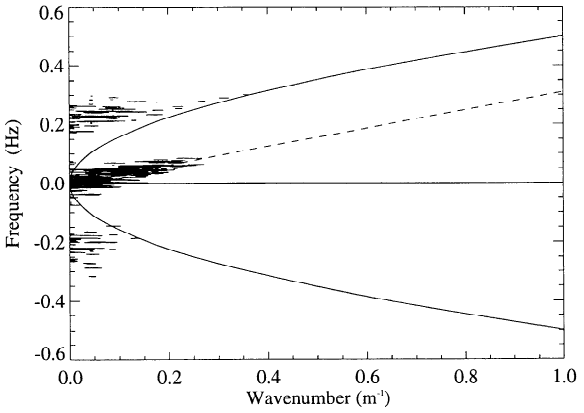

Figure 10. Contour plot of frequency-wavenumber spectrum of velocity using horizontal polarization. Little spectral power is present along the linear dispersion line (solid line). Nonlinear features making up the group line (dashed line) and its sidebands dominate.

shadowing may remove part of the Doppler spectrum, it cannot produce the strong enhancements of power and velocity that breaking does.

Features of interest in the two-dimensional spectrum (e.g., linear wave energy or group line) can be isolated with a band-pass filter in the f-k domain and then integrated in frequency (or wavenumber) to obtain the one-dimensional wavenumber (or frequency) spectrum. Figure 11a (solid line) shows the result of such an operation for the linear dispersive wave energy in Figure 9 using a 0.1-Hz-wide filter centered on the dispersion line. In a similar manner the dashed line shows the extraction of the group line. The equivalent frequency spectra are shown in Figure 11b. Due to the larger data record in time than in range, the wavenumber spectrum is obtained by integrating over a greater number of (frequency) points than the frequency spectrum and consequently emerges smoother but with less resolution. The frequency spectrum requires additional smoothing to obtain the same spectral stability. The spectra from the dispersion line data show the form expected from wind-wave spectra; they peak at 0.41 rad m^{-1} and 0.32 Hz. The higher-resolution frequency spectrum also shows a subsidiary peak in spectral power at 0.4 Hz. To obtain the actual wave height spectra, a further correction of $1/k$ or $1/\omega^2$ must be applied to transform from the velocity spectra in Figure 11 [*Plant et al.*, 1983].

The two-dimensional spectrum (Figure 9) provides a clear separation of the linear dispersive wave energy from other (nonlinear) effects: a separation which is not possible with a frequency spectrum at a fixed point or a wavenumber spectrum at an instant of time. If simultaneous spatial and temporal information had not been used, the calculated one-dimensional spectrum would include spectral power which was not due to the first-order linear dispersive wave energy. Our own experience highlights this danger, where a one-dimensional spectrum which was initially interpreted as being dominated by low frequency swell was, after using two-dimensional analysis, subsequently shown to be contaminated by nondispersive effects, particularly the group line. In shallow water where the group and phase velocities are equal, the separation of linear waves from the group line may not be so pronounced, since the group line will be a factor of 2 steeper and may merge into the dispersion line.

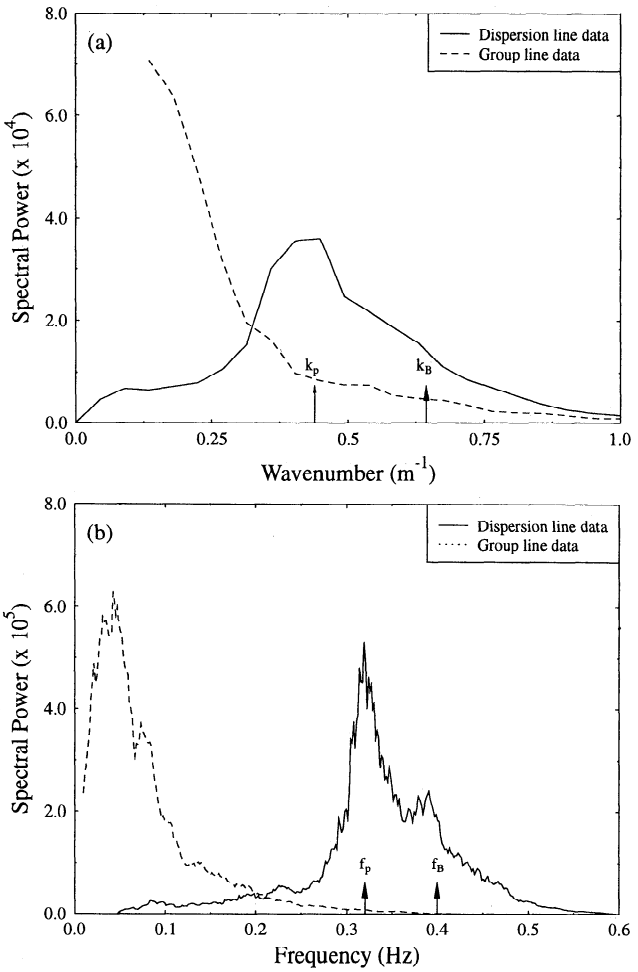

Figure 11. (a) Wavenumber spectrum obtained after filtering and integrating the two-dimensional spectrum over frequency. Here k_p is the spectral peak, and k_B is the predominant breaking wave wavenumber. (b) Frequency spectrum obtained after filtering and integrating over wavenumber. Here f_p is the spectral peak, and f_B is the predominant breaking wave frequency. A 0.1-Hz-wide filter was applied in a band about the theoretical dispersion curve (solid line) and about the group line (dashed line).

Since the nonlinear effects are significantly stronger using HH polarization, the data from marine radars (which are predominantly horizontally polarized) must be interpreted with care at low wavenumbers when attempting to derive wave height spectra. Evidence for this contamination is given by *Meadows et al.* [1988] and also *Hoogeboom et al.* [1986]. The group line may also explain the unusual low-frequency spectral density in the measurements of *Plant et al.* [1983]. A further consequence of the existence of nonlinearity is that a frequency spectrum cannot be converted to the wave number domain using the dispersion relation, or vice versa, as pointed out by *Barrick* [1986].

The distribution of spectral power along the group line indicates the dominant scales of occurrence of these nonlinear breaking and shadowing features. In an idealized situation of a narrow bandwidth wave group with a sinusoidal envelope, the group size is constant and the nonlinear breaking or shadowing would occur at the position of maximum wave amplitude, and hence slope, at the center of the envelope. These features would occur at fixed space and time intervals and propagate at the group velocity. This would give rise to a point on the frequency-wavenumber diagram corresponding to the repetition scales of the group, plus any higher harmonics also along this line. In this simple case the number of waves per group is also fixed and directly related to the group bandwidth. In a developing sea situation, a narrowband Gaussian description may be a more appropriate description of the wave field. In this case the probability density for the group envelope is Rayleigh distributed [*Longuet-Higgins*, 1984]. The distribution of group scales will be represented on the dispersion diagram by a scatter of spectral power at the appropriate scales but linked through the group velocity. A feature of the observed group line is that although there is a wide distribution in frequency (i.e., a large range in intervals between groups), the range of group velocities is relatively small, indicating a common narrowband origin.

The distribution in frequency can be seen more clearly as the dashed line in Figure 11b. The dominant frequency of breaking occurrence is offset from the origin, suggesting that there is a minimum to the frequency of group occurrence; that is, there is an upper limit to the length of groups. Note that the time series of velocity was sufficiently long to include the largest repetition interval, whereas there was insufficient spatial coverage to resolve the largest group spatial interval (Figure 11a). Since the group length is inversely related to the spectral bandwidth [*Longuet-Higgins*, 1984], this implies a minimum in the spectral width. This is consistent with the theoretical predictions for weakly nonlinear interactions for an inhomogeneous wind sea [*Janssen*, 1991]. From Figure 11b the central frequency of the group feature is 0.039 Hz, corresponding to a mean time between groups of 26 s. The 1/e repetition extremes correspond to intervals of 11 and 105 s. The peak period of the wave spectrum is 3.2 s. Therefore assuming the group line represents the spectrum of breaking occurrence, every 8.4th wave crest breaks; that is, the fraction of breaking wave crests is 0.12. This figure is of a similar order of magnitude to the data compiled by *Holthuijsen and Herbers* [1986, Figure 7] for this wind speed, although at the upper boundary of that data.

This discussion has centered on the frequency distribution of breaking. The spectral power density also provides information on the depth of modulation of velocity or backscattered power caused by the breaking or shadowing, compared with the modulation associated with Bragg scatter of the dispersive feature. Future work will aim to utilize this information to quantify the energy involved in wave breaking.

A consistent feature of the group line is that the slope or inferred group velocity corresponds to a wave of frequency f_B which is higher than the frequency of the peak of the wave height spectrum f_p. The slope of the group line in Figure 9 corresponds to waves in the band 0.4 ± .05 Hz, and this value of f_B is shown in Figure 11b with an arrow: it is 25% higher in frequency than f_p. If we interpret the group line as being dominated by the radar response to breaking waves, this result implies that the dominant breaking is due to waves at this higher frequency. Other data sets also show this characteristic of breaking well above the peak frequency.

Wave dissipation is an important source term in wave development models [e.g., *Hasselmann*, 1974; *Phillips*, 1985], but little experimental data are available on its

spectral distribution. In the simplest case, the dissipation /breaking is assumed to be simply proportional to the wave spectrum, $S(k)$. Then the mean frequency of the breaking waves can be obtained from the mean frequency of the wave height spectrum. Here its calculated value from the spectral moments is 0.34 Hz. This is above the spectral peak but still well below the group line mean frequency. Often a single threshold for breaking has been sought based on wave slope, though this has proved difficult [*Holthuijsen and Herbers*, 1986]. Converting the wave height spectrum to an equivalent form, $k\sqrt{S(k)}$, does give added emphasis to higher frequencies but still peaks below 0.4 Hz. Alternatively, *Hasselmann* [1974] introduced a coefficient with a quadratic frequency dependence. This gives added emphasis to higher frequencies but still does not produce the breaking centroid at 0.4 Hz. *Phillips* [1985] obtained a more strongly nonlinear term, proportional to $k^8S^3(k)$, based on a balance between source terms for an equilibrium spectrum. This form gives sufficient emphasis to 0.4 Hz in accord with our observations.

A further indicator of the scale of breaking can be obtained from the radar Doppler spectra. Within a single breaking event the plume velocity measured with HH polarization should be closely related to the phase velocity of the breaking waves (section 3.5). This velocity should provide a more unambiguous measure of scale than the instantaneous configuration of the ill-defined breaking water surface [*Phillips*, 1985]. Thus, returning to the Doppler spectra in Figure 4, we see that the HH upwind return peaked at a velocity of -2.2 m s^{-1}, while the spectral peak phase velocity was 3.3 m s^{-1}. If this Doppler spectrum resulted solely from a breaking plume moving at the phase velocity of the breaking waves, then the ratio of breaking frequency to peak frequency will equal the inverse of the ratio of phase velocities, 1.5. In a similar way the ratio obtained from the Doppler spectra corresponding to Figure 9 is 2.1. This is higher than the ratio deduced from the group velocity but may reflect the relaxation of the plume to slower velocities following the initiation of breaking. In a complementary experiment, *Ding and Farmer* [1994] have measured the speed of breaking events by tracking the acoustic sources associated with breaking waves. They infer that the mean breaking wave frequency is 1.3-2.2 times the dominant wave frequency. Recently, *Thorpe* [1993] argued that wave energy is fed into turbulent kinetic energy by breaking waves with frequencies up to 4 times the dominant spectral frequency. This was deduced on the basis that breaking waves near the spectral peak would provide more energy than is found from measurements of turbulent dissipation. The frequency of breaking waves deduced by Thorpe ($4f_p$) is significantly higher that the figure found here ($1.25f_p$). Subsequently, *Melville* [1994] improved this estimate by emphasizing the unsteady nature of wave breaking in the field and by introducing a shallow surface mixed layer with dissipation rates 1 to 2 orders of magnitude higher than used by Thorpe. Melville's characteristic speed of the breaking waves coresponds to frequencies in the range $1.6f_p$ to $2.5f_p$, in better agreement with the acoustic results and the radar results of this section.

5.4. Additional Nonlinear Features

We can obtain further detail from the two-dimensional spectrum by exaggerating the lower spectral density scales. This has been done in Figure 12 for backscattered power using vertical polarization. A component lying on the theoretical linear relationship for waves traveling in the opposite direction is now apparent. In the Antarctic experimental situation we ascribe this component to wave energy reflected from the ice edge. Integration of this component in a similar manner to that described in section 5.3 shows that the spectrum peaks at the same wavenumber as the incident arm of the dispersion curve (0.065 m^{-1}) and corresponds to a reflection coefficient of 5%.

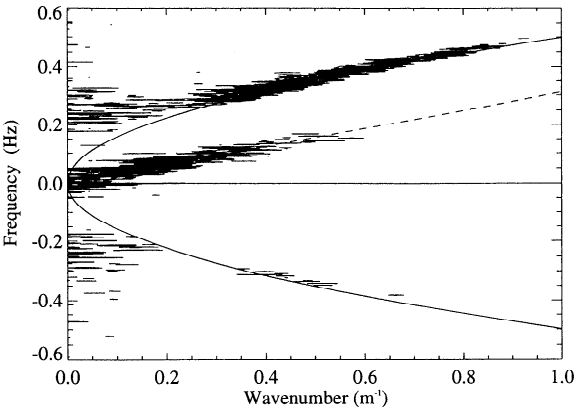

Figure 12. Contour plot of frequency-wavenumber spectrum of backscattered power using vertical polarization, on an exaggerated contour scale. In addition to spectral power along the linear dispersion line (solid line) and group line (dashed), a sideband feature and a small reflected component (bottom half of diagram) are apparent.

The lower contour levels also reveal a concentration of spectral densities at low wavenumbers separated from, but approximately parallel to, the group line with an axis intercept at zero wavenumber at $f = \pm 0.23$ Hz. The features have the appearance of sidebands to the group line. The peak of a wave group propagates at the group velocity but rather than behaving as a solid target, which would only give rise to spectral power along the group line, the breaking persists for only a fraction of a wave period and tends to repeat at twice the period of the dominant breaking waves T_B (section 4). Thus the propagation of the wave group (delineated by the propagation of breaking events) is further modulated at a period $2T_B$ giving rise to sidebands of the group line at a separation $\pm 1/2T_B$ ($\pm f_B/2$). These features would intersect the $k = 0$ axis at $f_B/2 = 0.2$ Hz, in broad agreement with the observed spectral power intersecting at $f = \pm 0.23$ Hz. A similar feature was reported by *Jacobsen and Eltoft* [1991] for delta-k radar studies of the ocean surface. They showed that it arose from group modulation in the nonlinear signal detection method used by dual-frequency radars.

6. Conclusions

We have described S band radar results which reinforce the well-established spiky nature of low grazing angle HH backscatter associated with breaking waves when the antenna is directed into the wind waves. This backscatter is accompanied by high velocities with large variance when compared with VV backscatter. However, the velocity difference between HH and VV reduces as the antenna azimuth is changed to the downwind direction. The VV azimuthal variation is consistent with Bragg dominated scatter plus a wind drift current. The averaged Doppler spectra for HH

downwind are also similar to those expected of Bragg scatter but with a small additional velocity offset. The upwind HH spectra, although intermittent, are distributed over velocities more typical of the underlying longer gravity wave phase velocities. Beneath the strong HH spike echoes, a more uniform background level of scatter can be distinguished between spikes. The mean velocity of this component is also larger than the VV Bragg velocity. The polarization ratio, the strong upwind/downwind asymmetry, and the intermittency of the HH returns favor the breaking plume model of *Wetzel* [1990].

Radar measurements provide a sensitive detector of wave breaking. Although a time series of HH scatter appears random at a fixed location, the combined range and time information reveals a well-defined pattern to the breaking in deep water. On the basis of the time intervals between breaking and the velocity of propagation, it is shown that wave group effects modulate the occurrence of breaking. When waves are fully resolved in space and time, group modulation can also be seen in the range-time display diagrams of both backscattered power and velocity. The two-dimensional frequency-wavenumber spectrum allows the separation of linear and nonlinear features. The frequency-wavenumber spectrum using VV polarization is usually dominated by linear wave energy satisfying the dispersion relation but can have a significant contribution along a line whose slope relates to the group velocity of the breaking waves. The slope of this line suggests that the dominant breaking wave frequency is significantly above the spectrum peak frequency, typically by 25%. The frequency-wave number spectrum provides quantitative information on the statistics of breaking and allows the breaking to be related to the background wave spectrum.

Acknowledgments. The authors wish to thank W. Ireland for technical support in the development of the radar. This research was supported by the New Zealand Foundation for Research, Science and Technology under contract CO1323 and the Office of Naval Research under grant N00014-93-1-0484.

References

Banner, M.L., and E.H. Fooks, On the microwave reflectivity of small-scale breaking water waves, *Proc. R. Soc. London A, 399,* 93-109, 1985.

Banner, M.L., and D.H. Peregrine, Wave breaking in deep water, *Annu. Rev. Fluid Mech., 25,* 373-397, 1993.

Barrick, D.E., FM-CW radar signals and digital processing, *Tech. Rep. ERL 283 WPL-26,* Natl. Oceanic and Atmos. Admin., Silver Spring, Md., 1973.

Barrick, D.E., The role of the gravity-wave dispersion relation in HF radar measurements of the sea surface, *IEEE J. Oceanic Eng., OE-11,* 286-292, 1986.

Ding, L., and D.M. Farmer, Observations of breaking surface wave statistics, *J. Phys. Oceanogr., 24,* 1368-1387, 1994.

Donelan, M., M.S. Longuet-Higgins, and J.S. Turner, Periodicity in whitecaps, *Nature, 239,* 449-451, 1972.

Donelan, M.A., J. Hamilton, and W.H. Hui, Directional spectra of wind-generated waves, *Philos. Trans. R. Soc. London A, 315,* 509-562, 1985.

Duncan, J.R., W.C. Keller, and J.W. Wright, Fetch and wind speed dependence of Doppler spectra, *Radio Sci., 9,* 809-819, 1974.

Farmer, D.M., and S. Vagle, On the determination of breaking surface distributions using ambient sound, *J. Geophys. Res., 93,* 3591-3600, 1988.

Farmer, D.M., C.L. McNeil, and B.D. Johnson, Evidence for the importance of bubbles in increasing air-sea flux, *Nature, 361,* 620-623, 1993.

Hasselmann, K., On the spectral dissipation of ocean waves due to white capping, *Boundary Layer Meteorol., 6,* 107-127, 1974.

Holthuijsen, L.H., and T.H.C. Herbers, Statistics of breaking waves observed as whitecaps in the open sea, *J. Phys. Oceanogr., 16,* 290-297, 1986.

Hoogeboom, P., J.C.M. Kleijweg, and D. van Halsema, Seawave measurements using a ship's radar, in *Proceedings of the International Geoscience and Remote Sensing Symposium '86, Zurich,* pp. 819-823, Inst. of Elec. and Electron. Eng., New York, 1986.

Irani, G.B., B.L. Gotwols, and A.W. Bjerkaas, The 1978 ocean wave dynamics experiment, in *Wave Dynamics and Radio Probing of the Ocean Surface,* edited by O.M. Phillips and K. Hasselmann, pp. 285-293, Plenum, New York, 1986.

Jacobsen, S., and T. Eltoft, The influence of wave groups on the dual-frequency Doppler spectrum: Experimental and theoretical approach, *Radio Sci., 26,* 831-845, 1991.

Janssen, P.A.E.M., On nonlinear wave groups and consequences for spectral evolution, in *Directional Ocean Wave Spectra,* edited by R.C. Beal, pp. 46-52, John Hopkins Univ. Press, Baltimore, Md., 1991.

Jessup, A.T., W.C. Keller, and W.K. Melville, Measurements of sea spikes in microwave backscatter at moderate incidence, *J. Geophys. Res., 95,* 9679-9688, 1990.

Jessup, A.T., W.K. Melville, and W.C. Keller, Breaking waves affecting microwave backscatter, 2., Dependence on wind and wave conditions, *J. Geophys. Res., 96,* 20,561-20,569, 1991.

Keller W.C., W.J. Plant, and G.R. Valenzuela, Observations of ocean breaking waves with coherent microwave radar, in *Wave Dynamics and Radio Probing of the Ocean Surface,* edited by O.M. Phillips and K. Hasselmann, pp. 285-293, Plenum, New York, 1986.

Lange, P., and H. Hühnerfuss, Drift responses of monomolecular slicks in wave and wind action, *J. Phys. Oceanogr., 8,* 142-150, 1978.

Lewis B.L., and I.D. Olin, Experimental study and theoretical model of high-resolution radar backscatter from the sea, *Radio Sci., 15,* 815-828, 1980.

Long, M.W., On a two-scatterer theory of sea echo, *IEEE Trans. Antennas Propag., AP-22,* 667-672, 1974.

Longuet-Higgins, M.S., The generation of capillary waves by steep gravity waves, *J. Fluid Mech., 16,* 138-159, 1963.

Longuet-Higgins, M.S., Statistical properties of wave groups in a random sea state, *Philos. Trans. R. Soc. London A, 312,* 219-250, 1984.

Lyzenga, D.R., A.L. Maffett, and R.A. Shuchman, The contribution of wedge scattering to the radar cross section of the ocean surface, *IEEE Trans. Geosci. Remote Sens., GE-21,* 502-505, 1983.

McGregor, J.A., E.M. Poulter, and M.J. Smith, A switching system for single antenna operation of an S-band FMCW radar, *Proc. Inst. Electr. Eng., 141,* 241-248, 1994.

Meadows, G.A., L.A. Meadows, L.L. Weishar, and M.L. Fields, DARTS (Digital Automated Radar Tracking System): Application to tidal inlet hydrodynamic studies, in *Lecture Notes on Coastal and Estuarine Studies,* vol. 29, edited by D.G. Aubrey and L. Weishar, pp. 169-185, Springer-Verlag, New York, 1988.

Melville, W.K., Energy dissipation by breaking waves, *J. Phys. Oceanogr., 24,* 2041-2049, 1994.

Melville, W.K., and R.J. Rapp, Momentum flux in breaking waves, *Nature, 317,* 514-516, 1985.

Melville, W.K., M.R. Loewen, F.C. Felizardo, A.T. Jessup, and M.J. Buckingham, Acoustic and microwave signatures of breaking waves, *Nature, 336,* 54-56, 1988.

Mitsuyasu, H., A note on the momentum transfer from wind to waves, *J. Geophys. Res., 90,* 3343-3345, 1985.

Phillips, O.M., Spectral and statistical properties of the equilibrium range in wind-generated gravity waves, *J. Fluid Mech., 156,* 505-531, 1985.

Phillips, O.M., Radar returns from the sea surface - Bragg scattering and breaking waves, *J. Phys. Oceanogr., 18,* 1065-1074, 1988.

Pigeon, V.W., Doppler dependence of radar sea return, *J. Geophys. Res., 73,* 1333-1341, 1968.

Plant, W.J., and W.C. Keller, Evidence of Bragg scattering in

microwave Doppler spectra of sea return, *J. Geophys. Res., 95,* 16,299-16,310, 1990.

Plant, W.J., W.C Keller, and A. Cross, Parametric dependence of ocean wave-radar modulation transfer functions, *J. Geophys. Res., 88,* 9747-9756, 1983.

Poulter, E.M., M.J. Smith, and J.A. McGregor, Microwave backscatter from the sea surface: Bragg scattering by short gravity waves, *J. Geophys. Res., 99,* 7929-7943, 1994.

Poulter, E.M., M.J. Smith, and J.A. McGregor, S-Band FMCW radar measurements of ocean surface dynamics, *J. Atmos. Oceanic Technol., 12,* 1271-1286, 1995a.

Poulter, E.M., M.J. Smith, and J.A. McGregor, The contribution of Bragg scattering to scatterometer signatures, *Int. J. Remote Sens., 16,* 2703-2711, 1995b.

Smith, S.D., Coefficients for sea surface wind stress, heat flux, and wind profiles as a function of wind speed and temperature, *J. Geophys. Res., 93,* 15,467-15,472, 1988.

Thorpe, S.A., On the clouds of bubbles formed by breaking wind-waves in deep water, and their role in air-sea gas transfer, *Philos. Trans. R. Soc. London A, 304,* 155-210, 1982.

Thorpe, S.A., Energy loss by breaking waves, *J. Phys. Oceanogr., 23,* 2498-2501, 1993.

Thorpe, S.A., and P.N. Humphries, Bubbles and breaking waves, *Nature, 283,* 463-465, 1980.

Trizna, D.B., J.P. Hansen, P. Hwang, and J. Wu, Laboratory studies of radar sea spikes at low grazing angles, *J. Geophys. Res., 96,* 12,529-12,537, 1991.

Trizna, D.B., J.P. Hansen, P. Hwang, and J. Wu, Ultra-wideband radar studies of steep crested waves with scanning laser measurements of wave slope profiles, *Dyn. Atmos. Oceans, 20,* 33-53, 1993.

Wetzel, L., On the origin of long-period features in low-angle sea backscatter, *Radio Sci., 13,* 313-320, 1978.

Wetzel, L.B., Electromagnetic scattering from the sea at low grazing angles in *Surface Waves and Fluxes: Current Theory and Remote Sensing,* vol. 2, edited by G.L. Geernaert and W.J. Plant, pp. 109-171, Kluwer Acad., Norwell, Mass., 1990.

Wetzel, L.B., A time domain model for sea scatter, *Radio Sci., 28,* 139-150, 1993.

Wright, J.W., A new model for sea clutter, *IEEE Trans. Antennas Propag., AP-16,* 217-223, 1968.

Wu, J., Wind-induced drift currents, *J. Fluid Mech., 68,* 49-70, 1975.

Wu, J., Sea-surface currents induced by wind and waves, *J. Phys. Oceanogr., 13,* 1441-1451, 1983.

J. A. McGregor, E. M. Poulter, and M. J. Smith, National Institute of Water and Atmospheric Research Ltd., P.O. Box 14901, Kilbirnie, Wellington, New Zealand. (e-mail: m.smith@niwa.cri.nz)

(Received September 13, 1994; revised February 3, 1996; accepted February 3, 1996.)